**Supporting Information**

# Polyaniline-functionalized jute fiber as a sustainable electrode for high-performance supercapacitors

*Md. Sanwar Hossain[1], Md Humayun Kabir[2]*, Md Yeasin Pabel[1], and Sabina Yasmin[1]**

[1]*Institute of National Analytical Research and Service (INARS), Bangladesh Council of Scientific and Industrial Research (BCSIR), Dhanmondi, Dhaka-1205, Bangladesh*
[2]*Institute of Food Science and Technology (IFST), Bangladesh Council of Scientific and Industrial Research (BCSIR), Dhanmondi, Dhaka-1205, Bangladesh*
*Corresponding author e-mail: (Sabina Yasmin) sabinayasmin@bcsir.gov.bd
*Corresponding author e-mail: (Md Humayun Kabir) humayunkabir@bcsir.gov.bd

**This file includes**

**S1.1 Repeated the electrochemical measurement**

The specific capacitance values of the electrode were evaluated at various scan rates ranging from 10 to 200 $mVs^{-1}$ using cyclic voltammetry. As shown in Table S1, the capacitance decreased with increasing scan rate due to limited ion diffusion at higher rates. at 10 $mVs^{-1}$, the electrode exhibited a maximum capacitance of $3860.70 \pm 204.63$ $Fg^{-1}$ at 10 $mVs^{-1}$ (mean ± SD, n = 3). Even at a higher scan rate of 200 $mVs^{-1}$, a respectable value of $2306.94 \pm 256.47$ $Fg^{-1}$ was retained, indicating excellent rate capability and electrochemical stability. The results demonstrate good reproducibility, as evidenced by the low standard deviations across the replicates.

**Table S1.** Variation of specific capacitance with scan rate (10–200 $mVs^{-1}$) for the JF/PANI electrode. The data are presented as mean ± standard deviation (n = 3)

| Scan rate ($mVs^{-1}$) | Exp. 1 | Exp. 2 | Exp. 3 | Mean ($F\ g^{-1}$) | SD ($F\ g^{-1}$) |
|---|---|---|---|---|---|
| 10 | 4137.86 | 3794.21 | 3650.02 | 3860.70 | ±204.63 |
| 20 | 3949.29 | 3365.00 | 3466.35 | 3593.55 | ±254.93 |
| 40 | 3689.29 | 3238.82 | 3240.17 | 3389.43 | ±212.03 |
| 60 | 3514.29 | 2932.42 | 2933.76 | 3126.82 | ±273.98 |
| 80 | 3346.43 | 2738.51 | 2739.86 | 2941.60 | ±286.26 |
| 100 | 3201.43 | 2619.44 | 2620.78 | 2813.88 | ±274.04 |
| 120 | 3087.86 | 2486.84 | 2488.18 | 2687.62 | ±283.01 |
| 140 | 2975.46 | 2355.01 | 2399.36 | 2576.61 | ±282.61 |
| 160 | 2855.89 | 2250.09 | 2295.43 | 2467.14 | ±275.51 |
| 180 | 2760.71 | 2206.34 | 2207.68 | 2391.58 | ±261.02 |
| 200 | 2669.64 | 2124.91 | 2126.25 | 2306.94 | ±256.47 |

Additionally, the specific capacitance of the JF/PANI electrode was also evaluated at different current densities ranging from 5 to 50 $Ag^{-1}$ using galvanostatic charge discharge (GCD) tests. As shown in Table S2, the specific capacitance gradually decreased with increasing current density due to reduced ion diffusion and limited active site utilization at higher current. At a current density of 5 $Ag^{-1}$, a high capacitance of $3485.68 \pm 111.24\ Fg^{-1}$ was observed, which remained at $3052.35 \pm 119.57 Fg^{-1}$ even at 50 $Ag^{-1}$. The low standard deviations across the trials indicate good reproducibility and stability of the electrode material.

Table S2. Specific capacitance at various current densities with mean ± SD (n = 3).

| Current density (Ag-1) | Exp. 1 | Exp. 2 | Exp. 3 | Mean ($Fg^{-1}$) | SD ($Fg^{-1}$) |
|---|---|---|---|---|---|
| 5 | 3642.86 | 3401.43 | 3412.76 | 3485.68 | ±111.24 |
| 10 | 3498.57 | 3331.43 | 3348.47 | 3392.82 | ±75.10 |
| 15 | 3437.14 | 3230.00 | 3287.04 | 3318.06 | ±87.36 |
| 20 | 3397.14 | 3194.29 | 3247.04 | 3279.49 | ±85.94 |
| 25 | 3350.00 | 3571.43 | 3199.90 | 3373.78 | ±152.60 |
| 30 | 3321.43 | 3298.57 | 3171.33 | 3263.78 | ±66.03 |
| 35 | 3285.00 | 2900.00 | 3134.90 | 3106.63 | ±158.44 |
| 40 | 3268.57 | 2948.57 | 3118.47 | 3111.87 | ±130.72 |
| 45 | 3233.57 | 2932.14 | 3083.47 | 3083.06 | ±123.06 |
| 50 | 3200.00 | 2907.14 | 3049.90 | 3052.35 | ±119.57 |

## S2.1 Optimization structure of JF and PANI

The structure illustrates the extended chain conformation of PANI in its emeraldine base form, featuring alternating benzenoid and quinoid units. Carbon atoms are shown in grey, hydrogen atoms in white, and nitrogen atoms in blue. The geometry reveals a semi-flexible backbone with slight curvature, which is typical due to the delocalization of π-electrons along the conjugated system. The nitrogen atoms are positioned in para-positions within the polymer chain, playing a critical role in the electronic and redox properties of PANI. This optimized structure provides valuable insight into the electronic distribution and structural stability of the polymer, which is essential for its application in sensors, supercapacitors, and conductive materials in Fig. S1.

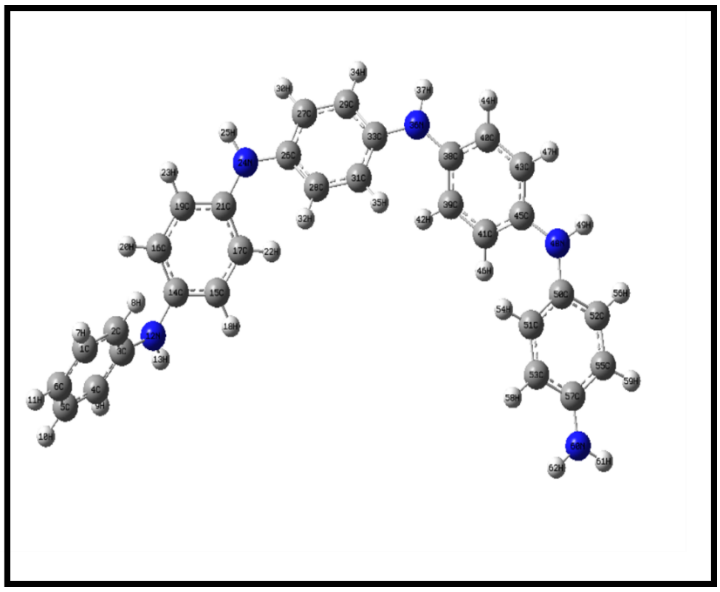

**Figure S1.** Optimized geometry of PANI using DFT B3LYP/6-311Glevel of theory.

To gain deeper insight into the molecular interactions and electronic behavior of the PANI–cellulose composite, Density Functional Theory (DFT) calculations were carried out using the B3LYP functional with the 6-311G basis set [1][2]. The optimized molecular structure of the PANI–cellulose complex (Fig. S2) clearly exhibits favorable interactions between the cellulose hydroxyl groups and the nitrogen sites of PANI chains. Multiple hydrogen bonds were observed,

primarily between the –OH groups of cellulose and the imine (=N–) and amine (–NH–) groups of PANI. These interactions play a critical role in anchoring the polymer chains onto the cellulose backbone, thereby enhancing interfacial adhesion and mechanical stability of the composite material.

Furthermore, π–π stacking interactions between the aromatic rings of PANI and the glucose units of cellulose were also predicted, contributing additional stabilization to the hybrid system. This molecular alignment facilitates efficient electron delocalization throughout the structure, a key parameter in achieving high electrochemical conductivity and capacitance. Fig.S3 presents the optimized structure of pristine PANI, displaying extended conjugation along the polymer backbone and localized electron density at the nitrogen sites, which are crucial for its redox activity in energy storage applications.

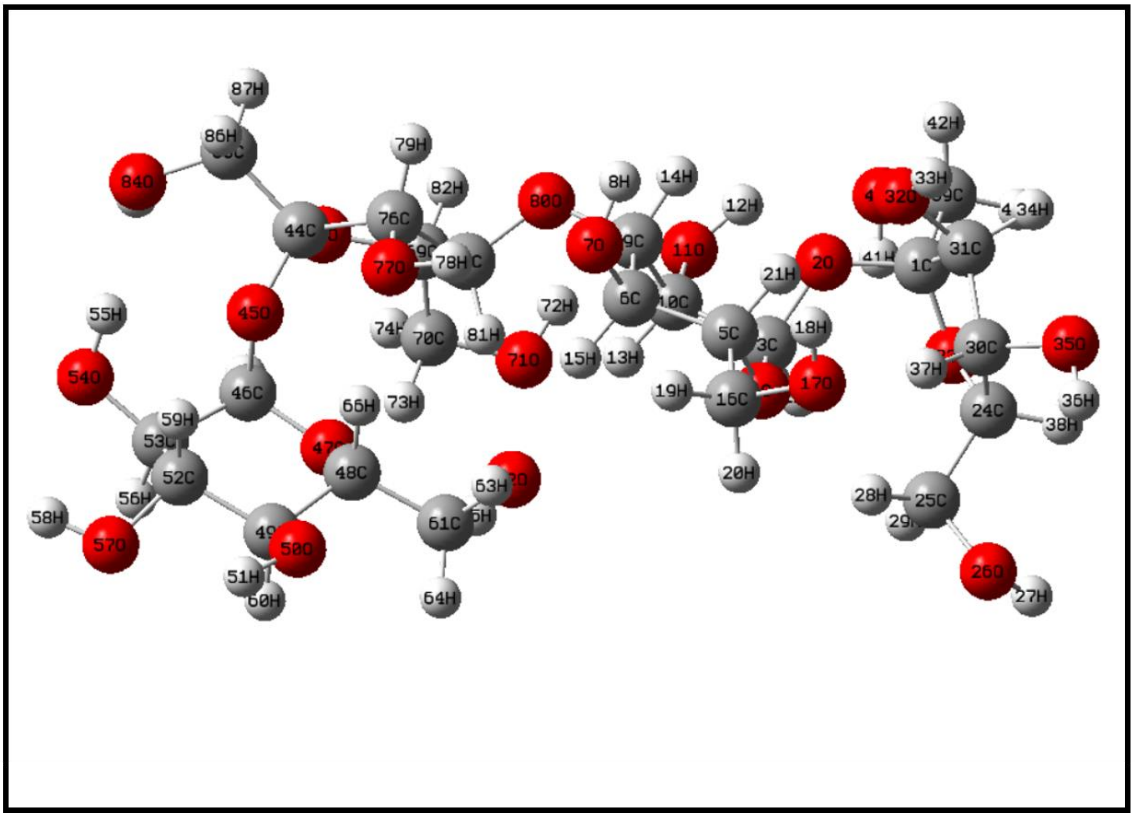


**Figure S2.** Optimized geometry of PANI using DFT B3LYP/6-311Glevel of theory

**Table. S3.** Selected Bond Lengths, Bond Angles, and Dihedral Angles of Compounds PANI and PANI-cellulose Calculated at the APFD/6- 311Level of theories

| Species | Bond distances (Å) | Cellulose | PANI-cellulose | Bond angle (°) | Cellulose | PANI-cellulose |
|---|---|---|---|---|---|---|
| Cellulose | O97-H98 | 0.9808 | 0.984 | C106-C145-O146 | 110.513 | 111.321 |
| | O102-C101 | 1.455 | 1.428 | H74-O73-C72 | 112.577 | 110.578 |
| | O130-C131 | 1.5015 | 1.466 | C63-C101-O102 | 110.498 | 111.697 |
| | O146-H147 | 0.9805 | 0.992 | C71-O142-C173 | 119.187 | 117.925 |
| | O73-H74 | 0.9914 | 1.008 | C108-O107-C106 | 124.340 | 122.071 |
| | **Bond distances (Å)** | **PANI** | **PANI-celluose** | **Bond angle (°)** | **PANI** | **PANI-cellulose** |
| PANI | N12-C3 | 1.401 | 1.418 | **C3-C4-N12** | 1188.562 | 117.453 |
| | N12-H13 | 1.009 | 1.027 | C53-57-60 | 120.021 | 119.479 |
| | C3-C4 | 1.412 | 1.414 | C2-C1-C6 | 121.121 | 120.859 |
| | C57-C55 | 1.409 | 1.405 | C31−C33−N36 | 123.073 | 118.600 |
| | C21-N24 | 1.403 | 1.426 | **Dihedral angle (°)** | | |
| | N60−C57 | 1.388 | 1.442 | C51−C50−N48-C45 | 36.131 | 29.004 |
| | C33-N36 | 1.404 | 1.443 | N60-C57−C55-C52 | 179.390 | 173.229 |
| | N60-H62 | 1.004 | 1.018 | C38−N36−C33-C31 | 21.875 | 76.147 |

The optimized geometric parameters of PANI, cellulose, and the PANI–cellulose complex, calculated at the APFD/6-311 level of theory, reveal notable structural changes upon complex formation[5]. In cellulose, several bond distances slightly changed, such as the O97–H98 bond increasing from 0.9808 Å to 0.984 Å and the O102–C101 bond shortening from 1.455 Å to 1.428 Å, indicating hydrogen bonding and molecular reorganization. Bond angles also shifted, including C106–C145–O146 increasing from 110.513° to 111.321°, and C63–C101–O102 from 110.498° to 111.697°, suggesting distortion near the interaction sites. In the PANI structure, the N12–C3 bond length elongated from 1.401 Å to 1.418 Å, while the N60–C57 bond increased from 1.388 Å to 1.442 Å, confirming interaction-induced strain. Correspondingly, bond angles like C3–C4–N12 and C31–C33–N36 decreased slightly. Significant changes were also observed in dihedral angles, such as C51–C50–N48–C45 shifting from 36.131° to 29.004°, and C38–N36–C33–C31 from 21.875° to 76.147°, indicating conformational twisting. These variations in bond lengths, bond angles, and dihedral angles support the presence of strong interfacial interactions—primarily hydrogen bonding—between PANI and cellulose, which enhance the structural stability and functionality of the composite system.

The mapped electrostatic potential (ESP) surfaces reveal significant charge accumulation near the nitrogen atoms in PANI and the oxygen atoms in cellulose, confirming the sites of strong electrostatic interaction[3]. These findings suggest that the incorporation of cellulose not only supports the structural integrity of PANI but also facilitates enhanced charge transport pathways and ion diffusion during the charge/discharge processes in supercapacitors. Overall, the theoretical results from DFT strongly correlate with experimental observations of high specific capacitance, making the PANI–cellulose composite a promising material for green and high-performance energy storage devices.

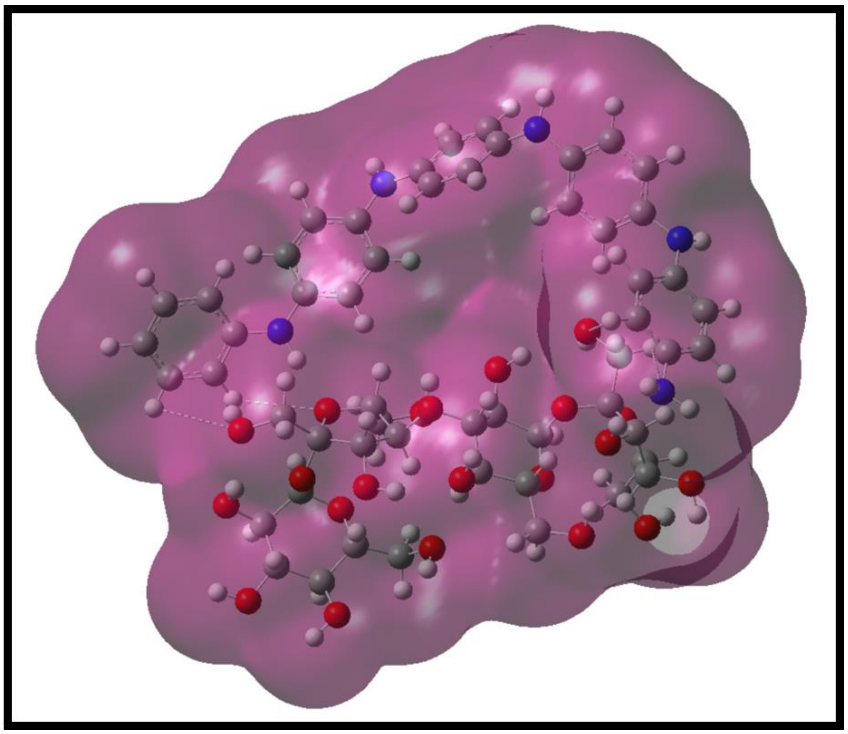

**Figure S3.** Electron density calculation of PANI-cellulose using DFT B3LYP/6-311level of theory.

## S2.1 Interaction Energy calculation

The interaction between polyaniline (PANI) and cellulose was investigated using density functional theory (DFT) calculations. The total electronic energies of PANI, cellulose, and the PANI–cellulose complex were found to be –1432.870 Hartree, –2518.5833 Hartree, and –3951.473 Hartree, respectively. The interaction energy was calculated using Equation (1)[4]:

$$\Delta E_{int} = E_{product} - (E_{reactant1} + E_{reactant2}) \quad (1)$$

Which corresponds to –51.722 kJ/mol. This negative interaction energy confirms a thermodynamically favorable and moderately strong binding between PANI and cellulose, as shown in Equation (2):

$$PANI + cellulose = PANI - cellulose \quad (2)$$

Additionally, the dipole moment of the PANI–cellulose complex (8.036 D) was lower than that of cellulose alone (9.188 D), suggesting that complex formation leads to charge redistribution and potential molecular alignment. The interaction energy trends further confirm the theoretical prediction that larger PANI models exhibit enhanced affinity for cellulose, supporting the hypothesis that molecular size and structure contribute significantly to the stability and strength of interfacial interactions in the composite system. These results highlight the potential of PANI–cellulose composites in electrochemical applications, especially where interfacial interactions play a critical role.

**Table S4.** Energy calculation of normal PANI-cellulose.

| Species | Energy (Hartree) | Dipole moment | Interaction Energy | |
|---|---|---|---|---|
| PANI | -1432.870 | 2.878 | Hartree | Kj/mol |
| Cellulose | -2518.5833 | 9.188 | | |
| PANI-Cellulose | -3951.473 | 8.0360 | -0.0197 | -51.722 |

**Table S5.** Hydrogen bonding between PANI and JF

| Donor Atom | Acceptor Atom | Interaction Type | Distance (Å) |
|---|---|---|---|
| H46 (PANI) | O102 (Cellulose) | O–H···O | 2.22 |
| H18 (PANI) | O138 (Cellulose) | O–H···O | 2.94 |
| H18 (PANI) | O138 (Cellulose) | O–H···O | 2.00 |
| H96 (Cellulose) | O97 (Cellulose) | O–H···O | 2.31 |
| H22 (PANI) | O73 (Cellulose) | O–H···O | 4.37 |
| H9 (PANI) | O146 (Cellulose) | O–H···O | 3.25 |
| H96 (Cellulose) | N60 (PANI) | N···H–O | 2.91 |
| H95 (Cellulose) | N60 (PANI) | N···H–O | 2.13 |
| H147 (Cellulose) | N12 (PANI) | N···H–O | 3.38 |
| H149 (Cellulose) | N12 (PANI) | N···H–O | 3.26 |

## Reference


[1] S. Song, S. Vuckovic, E. Sim, K. Burke, Density-Corrected DFT Explained: Questions and Answers, J Chem Theory Comput. 18 (2022) 817.

[2] N. Tańska, DFT study of low-energy electron interaction with pyridine, pyrazine and their halo derivatives, The European Physical Journal D. 75 (2021) 132. https://doi.org/10.1140/epjd/s10053-021-00137-0.

[3] H. Ullah, A.U.H.A. Shah, S. Bilal, K. Ayub, DFT study of polyaniline NH3, CO2, and CO gas sensors: Comparison with recent experimental data, Journal of Physical Chemistry C. 117 (2013) 23701–23711. https://doi.org/10.1021/jp407132c.

[4] B.B. Laird, R.B. Ross, T. Ziegler, Density-Functional Methods in Chemistry : An Overview Density-functional theory ( DFT ), in its various forms , has become an important research tool for chemists , physicists and materials scientists . Its development in recent years has proceeded along , (1996) 1–17.

[5] D.W. Boukhvalov, DFT modeling of the covalent functionalization of graphene: from ideal to realistic models, RSC Advances. 3 (2013) 7150–7159. https://doi.org/10.1039/C3RA23372C.